# Lipid bilayers determine the allostery but not intrinsic affinity of cAMP binding to pacemaker channels

Vinay Idikuda[1]†, Susovan Roy Chowdhury[1]†, Yongchang Chang[1], Qian Ren[5], Huan Bao[5], Randall H. Goldsmith[3], Baron Chanda*[1,3,4]

**Affiliations:**
[1] Department of Anesthesiology, Washington University in St. Louis; Saint Louis, MO 63110.
[2]Department of Chemistry, University of Wisconsin-Madison; Madison, WI 53706.
[3] Department of Biochemistry and Molecular Biophysics, Washington University School of Medicine; Saint Louis, MO, USA.
[4]Department of Neuroscience, Washington University School of Medicine; Saint Louis, MO, USA.
[5]Department of Molecular Physiology and Biological Physics, University of Virginia; 480 Ray C Hunt Drive, Charlottesville, 22903, Virginia, USA.
* Corresponding author: E-mail: bchanda@wustl.edu
† These authors contributed equally

**Abstract:** In the human heart, the binding of cyclic adenosine monophosphate (cAMP), a second messenger, to hyperpolarization and cyclic nucleotide-gated (HCN) regulates the automaticity of pacemaker cells. Recent single-molecule binding studies show that cAMP bound to each subunit of purified tetrameric HCN channels independently, in contrast to findings in cells. To explore the lipid membrane's role in cAMP regulation, we reconstituted purified human HCN channels in various lipid nanodiscs and resolved single molecule ligand-binding dynamics. Our measurements show that lipid membranes promote cooperative binding of cAMP to HCN channels without altering the intrinsic binding affinity. Cryo-EM structures of HCN channels in lipid nanodiscs reveal enhanced inter-subunit interactions, underscoring the fundamental role of lipid membranes in amplifying the gating sensitivity of ion channels.

## Introduction:

HCN, or pacemaker channels, are a distinct subclass of voltage-gated ion channels that are activated by membrane hyperpolarization and modulated by the intracellular second messenger cAMP(*1-5*). By integrating electrical and chemical signals, HCN channels play a critical role in regulating the rhythmic firing of cardiac and neuronal action potentials(*6, 7*). Each subunit of a tetrameric HCN channel contains a single cAMP binding site in its intracellular cyclic nucleotide-binding domain (CNBD). The binding of cAMP allosterically modulates channel gating, enhancing macroscopic current and accelerating activation kinetics(*8*).

Despite the essential role of cAMP in pacemaking, the mechanisms underlying cAMP-dependent gating of HCN channels remain controversial. Electrophysiology and patch-clamp fluorometry studies suggest that HCN channels function as dimer-of-dimers, with higher binding affinities for the first and third ligation states compared to the unbound or doubly-bound states(*9-15*). In contrast, cAMP binding to isolated CNBDs promotes tetramerization rather than dimerization(*16*). This discrepancy likely stems from issues of parameter identifiability in ensemble measurements(*17*). These challenges can be addressed using single-molecule approaches that directly measure microscopic equilibrium parameters(*17, 18*). However, detecting individual ligand binding events at concentrations above 10 nM is difficult due to the increased background from free fluorescent ligands(*19-21*). Recently, White et al. utilized zero-mode waveguides (ZMWs) to demonstrate that purified HCN channels bind all four cAMP molecules

independently(*22, 23*). ZMWs reduce the excitation volume by three orders of magnitude compared to conventional TIRF microscopy, enabling the study of fluorescent ligand binding dynamics at micromolar concentrations(*24-29*).

Although isolated HCN channels bind cAMP molecules independently, it remains unclear whether extrinsic factors, such as surrounding lipids, modulate ligand binding in cellular environments. High-resolution structures of detergent-solubilized HCN channels reveal bound lipid densities consistent with previous functional studies(*30, 31*). However, a vast of majority of the surrounding lipids, known as solvating lipids, interact transiently with integral membrane proteins(*32-34*). They are replaced by detergents upon solubilization and are not resolved in the high-resolution structures. While the influence of specific lipids or physical properties of the bilayer on channel structure and function has been extensively studied(*31, 35-39*), the role of these solvating lipids vis-a-vis other membrane mimetics is less understood. Since most structures of membrane signaling proteins, such as ion channels and GPCRs, are solved in detergents(*40, 41*), it is crucial to understand how these environments differ to accurately interpret functional mechanisms and guide structural studies.

To address these questions, we used HCN channels which are uniquely suited for studying ligand-dependent gating energetics at single molecule resolution in both detergents and lipid environment(*22, 42*). Here, we combined single-molecule ligand-binding studies with single-particle cryo-EM to examine HCN1 and HCN4 channels in lipid nanodiscs of varied composition compared them to widely used cryo-EM detergents. Our single-molecule studies reveal that, in contrast to detergents, lipid bilayers enhance cAMP binding cooperativity without altering the intrinsic binding affinity, which corresponds to the binding affinity of the first cAMP molecule. Cryo-EM analysis further shows that structural rearrangements in lipid nanodiscs promote intersubunit interactions. These findings provide new insights into how lipid bilayers modulate the quaternary structure and allosteric regulation of pacemaker ion channels.

**Results:**

***fcAMP binds cooperatively to HCN1 in nanodiscs***

To investigate whether lipid bilayers influence the ligand-binding dynamics of HCN1 channels, we isolated and purified heterologously expressed HCN1 channels using glyco-diosgenin (GDN) detergent. A portion of these purified channels was reconstituted into soy polar lipid nanodiscs by mixing the HCN1 protein with the scaffold protein MSP2N2 and phospholipids in a 1:2.5:200 ratio (Fig. 1A, Table 1). Reconstitution was validated through size exclusion chromatography and SDS-PAGE analysis (Fig. 1B), with tetrameric assembly confirmed via GFP photobleaching (fig. S2).

We measured ligand binding by immobilizing purified channels—either in detergent micelles or lipid nanodiscs—onto zero-mode waveguides (ZMWs) and introducing the fluorescent ligand fcAMP (DY-547-cAMP) (Fig. 1C). To ensure single-occupancy of ZMWs, protein concentration was adjusted based on Poisson dilution statistics as previously described(*43*). Ligand binding events were measured across a range of fcAMP concentrations using micromirror total internal reflection fluorescence (TIRF) microscopy(*44*). Fluorescence intensity-time (FT) traces were analyzed using autoDISC(*23, 45*) to identify bound and unbound states (Fig. 1D-I, fig. S3). Control experiments confirmed the absence of nonspecific binding, as demonstrated by no detectable ligand binding in the absence of HCN channels and by the competitive displacement of fcAMP with excess non-fluorescent cAMP at the end of each experiment (fig. S4).

Our results revealed that channels in nanodiscs exhibited a higher frequency of multi-ligand bound states (three or four fcAMP molecules bound) compared to the singly bound state, particularly at lower fcAMP concentrations (Fig. 1D-E, Fig. 1G-H). To assess cooperativity in binding, we normalized the time spent by fcAMP in each ligation state (state occupancy) to the expected value from a binomial distribution under the assumption of independent and identical binding sites. When ligand binding is independent, the ratio of observed to expected occupancies is 1. For HCN1 channels in nanodiscs, occupancy probabilities deviated significantly from binomial predictions, especially in high-occupancy states across all concentrations tested (Fig. 1J, fig. S7B, Table S10). For instance, at 50 nM fcAMP, the fourth bound state showed a deviation exceeding 25-fold. This effect diminished at higher fcAMP concentrations (2-5-fold deviation), likely due to saturation. In contrast, channels in detergent micelles displayed binding distributions consistent with independent binding (Fig. 1K, fig. S7A, Table S11), consistent with previous observations(*22*).

Using a sequential binding model, we calculated bound probabilities for each ligation state at various concentrations and generated ensemble binding curves from the single-molecule data. A bound probability of 1.0 indicates complete occupancy of all binding sites by fcAMP. From these probabilities, we determined the microscopic equilibrium constants for each transition (see Methods). Using the Adair equation(*46*) , we constructed binding curves (Fig. 1L). HCN1 channels in nanodiscs showed a three-fold increase in binding affinity compared to those in detergent micelles (Fig. 1L, black vs. red).

Overall, these results demonstrate that fcAMP binding to HCN1 channels in nanodiscs exhibits positive cooperativity, in contrast to the independent binding observed in detergent micelles.

***Lipid bilayers influence allostery not affinity***

We wondered whether the cooperativity observed in HCN1 channels reconstituted in soy polar lipids was influenced by the specific lipid species used. Phospholipids are key regulators of many ion channels in biological membranes(*47-52*), and recent studies(*31*) have shown that negatively charged phospholipids modulate HCN channel activity. To test this, we compared two lipid conditions: a native lipid composition (porcine brain polar lipid extract) and a simpler neutral lipid system (POPC/POPE in a 3:1 ratio). HCN channels exhibited robust binding activity at all concentrations in both brain polar lipid and POPC/POPE nanodiscs (Fig. 2A and B, fig. S5), consistent with observations in soy polar lipid nanodiscs.

Using idealized FT traces, we determined state occupancies for each ligation state across the concentration range and normalized them to expected values based on an independent binding model. In both brain polar lipids (Fig. 2C, top) and POPC/POPE (Fig. 2C, bottom), HCN1 state occupancies deviated from the expected values, mirroring trends observed in soy polar lipids. These results show that fcAMP binding to HCN1 is not independent.

To further explore this, we developed and optimized an unconstrained sequential binding model (Fig. 2D) and calculated equilibrium rate constants for each fcAMP binding step. The results showed a monotonic increase in rate constants across all lipid nanodisc types (Fig. 2G, red, blue, green, and tables S28, S29, S30). These findings indicate that fcAMP binding is cooperative in lipid environments, regardless of lipid origin or charge, but not in detergent-solubilized channels.

Next, we examined whether lipid-induced cooperativity arises from changes in agonist binding affinity or subsequent allosteric transitions. We analyzed unbound-bound-unbound (UBU) dwell time distributions for singly bound states, avoiding confounding effects from the binding of new ligands or unbinding of previously bound ones(*22*). Consistent with our prior work, maximum

likelihood estimations of UBU dwell time distributions for HCN1 were well described by two exponentials at all fcAMP concentrations (Fig. 2E and 2F, fig. S9A and B, fig. S10A and B, and tables S19, S20, S21, S22). This revealed that each subunit undergoes isomerization to a secondary conformation or flip state(*22*).

Importantly, these biexponential fits were consistent across detergent and nanodisc samples, and their weighted time constants were similar in all conditions (Fig. 2H and tables S19, S20, S21, S22). These results suggest that the lipid environment does not alter the intrinsic affinity of fcAMP for its binding site or the time spent in the initial bound state. Instead, lipids influence downstream allosteric transitions and the energetics of higher-order ligand-binding steps.

***Lipid bilayers confer cooperativity on HCN4***

Recent findings have demonstrated that the structure and function of certain membrane proteins depend on nanodisc size(*53-55*). While MSP2N2 nanodiscs have an average diameter of 15 nm, their size distribution is broad and influenced by the reconstituted protein. To examine whether nanodisc size impacts the cooperativity of ligand binding, we used circular nanodiscs with uniform sizes across a wide temperature range and minimal dependence on the reconstituted protein(*56, 57*). Spy-catcher and spy-tag MSPs were purified (fig. S1C and S1, F-I) to generate circular nanodiscs of 11 nm and 30 nm using soy polar lipids. Heatmap representations of FT traces revealed strong ligand-binding activity for both nanodisc types (Fig. 3A and fig. S6). Even at the lowest tested concentration (50 nM fcAMP), higher-order ligation states were observed, contrasting with detergent-solubilized samples.

Plots comparing observed and expected state occupancies for unbound and various bound states deviated from a binomial distribution, indicating non-independent binding (Fig. 3B, fig. S8, B and C, fig. S10, C and D, and tables S23, S24). Using the unconstrained sequential binding model in Fig. 2D, we extracted microscopic equilibrium constants for each of the four binding steps from idealized FT traces (Fig. 3C). Consistent with data from MSP2N2 nanodiscs, HCN1 reconstituted in both 11 and 30 nm circular nanodiscs exhibited positive cooperativity. Notably, the strongest cooperativity was observed in 30 nm nanodiscs, where the microscopic equilibrium constants for the third and fourth ligation states were nearly identical (Fig. 3C, blue). This finding aligns with functional data indicating that 60% cAMP occupancy is sufficient for maximal channel activation(*11*).

To determine whether this effect is generalizable to other HCN channels, we expressed and purified a C-terminal truncated, GFP-tagged human ortholog of HCN4 (fig. S1, J, K, L), which is approximately four times more sensitive to cAMP than HCN1(*58*). These channels were solubilized in GDN (Glyco-diosgenin), with a portion reconstituted in soy polar lipid nanodiscs using MSP2N2 as the MSP. Heatmap representations of FT traces showed that HCN4 ligand-binding activity in detergent micelles was lower than in soy polar lipids (Fig. 3D). In detergent micelles, the ratios of observed to expected occupancies for various ligation states were close to one, consistent with independent ligand-binding events (Fig. 3E, left). By contrast, observed occupancies in soy polar lipids deviated from independence (Fig. 3E, right), resembling HCN1 channels reconstituted in nanodiscs (fig. S12, A and B, table S16, S17).

Similar to HCN1 and HCN2(*22*), UBU dwell-time analysis of HCN4 revealed that the channel undergoes secondary isomerization into a flip state (fig. S12, C and D, and tables S16, S17, S26, and S27). Importantly, extracted microscopic equilibrium constants for each ligation step indicated that binding of the second and subsequent ligands is more favorable in channels reconstituted in nanodiscs than in detergent-solubilized channels (Fig. 3F, tables S35 and S36). Thus, as observed

with HCN1 isoforms, ligand binding in HCN4 channels reconstituted in lipid bilayers exhibits positive cooperativity, whereas channels reconstituted in detergent micelles exhibit independent binding.

***HCN1 shows cooperativity in native membranes***

Reconstituting membrane proteins in nanodiscs requires solubilizing both the target protein and lipids in detergent—in this case, GDN and CHAPS, respectively. Although we use BioBeads to remove most, if not all, detergent, we wondered whether exposure to detergent during purification might irreversibly alter the channel gating energetics. Additionally, we considered whether symmetrical bilayers in nanodiscs might affect the proteins differently compared to the asymmetric bilayers of native membranes.

To address whether native membranes support ligand-binding cooperativity, we employed detergent-free nanodiscs (DeFrNDs), which circumvent the need for protein solubilization and reconstitution steps(*59*). These nanodiscs are a novel class of engineered membrane scaffold peptides, derived from apolipoprotein A mimetic peptides, that facilitate the direct extraction of cell membranes as nanoscale membrane discoids (Fig. 4A). The HCN1-encapsulated discoids were then isolated through affinity purification.

HCN1 channels extracted into DeFrNDs directly from HEK cells exhibited robust ligand-binding activity, as evidenced by a high binding activity and substantial occupancy of higher ligation states at low concentrations (Fig. 4B, fig. S13A). Similar to HCN channels in detergents and nanodiscs, HCN1 channels in DeFrNDs showed UBU dwell time distributions with two time constants, indicating isomerization occurs after ligand binding (Fig. 4E, table S34). Furthermore, the observed state occupancies deviated significantly from expected binomial distributions (Fig. 4C, table S18), and microscopic equilibrium constants derived from globally fitted FT traces at all concentrations confirmed cooperativity (Fig. 4D, fig. S13B). Thus, HCN1 channels in DeFrNDs exhibit positive cooperativity comparable to that observed in reconstituted nanodiscs following detergent solubilization.

***Lipid bilayers facilitate inter-subunit coupling***

To determine whether lipid bilayers and detergent micelles differentially affect the structure of HCN channels, we reconstituted human HCN1 in circular nanodiscs and compared the single-particle cryo-EM structure to those obtained with detergent(*60*). Due to strong orientation bias, non-tilted imaging did not produce successful 3D maps. Therefore, we collected 30° tilt series data and combined them with a small fraction of particles from a non-tilted sample containing 0.2 mM fluorinated fos-choline to further reduce orientation preference caused by protein accumulation at the air-water interface.

The resulting map closely resembles the closed channel conformation in detergent micelles (Fig. 5A, figs. S14 and S15). Using the closed-state structure as the starting model, we built a structural model for hHCN1-nanodisc. Supplemental videos show the HCN1 structure transitioning from detergent to nanodisc, highlighting primary changes in inter-subunit interfaces. These include shortening the distances between the S4-S5 loop and the C-linker, as well as between the HCN domain and the CNBD (movies S1 and S2). This is further illustrated in Fig. 5C, which superimposes the hHCN1-nanodisc structure onto the hHCN1-detergent structure. Upward movement of the C-linker A’ and B’ and the CNBD domain in the nanodisc model resulted in an average decrease of ~1Å between these regions compared to the detergent model.

Fig. 5D shows zoomed-in views of two inter-subunit interfaces where structural deviations between the two conformations are observed. Narrowing of the cleft at the interface comprising the S4-S5 loop, HCN domain, and CNBD from the neighboring subunit is evident in the surface model of the nanodisc structure (Fig. 5C). Similar narrowing of the cleft was reported in the recently published structure of human HCN1 in PC:PE:PS lipid nanodiscs(*61*) (PDB: 8UC8) (fig. S16). Fig. 5D highlights more complex changes in the inter-subunit interface between the CNBD and C-linker region. In the nanodisc structure, the C' and D' helices of the C-linker are further from the A' and B' helices of the neighboring C-terminal domain but closer to the β-roll of the CNBD in the adjacent subunit. In these regions, more contact pairs are formed in the nanodisc structure (fig. S17).

These changes cannot be attributed to overall length compaction, a phenomenon often linked with severe orientation bias in cryo-EM studies, as the overall length of HCN1 in the nanodisc is nearly identical to that in detergent. Moreover, some structural changes in the nanodisc sample involve movements inconsistent with longitudinal compaction. Another global difference observed is the slight expansion of the transmembrane domain (by 1.3Å in outer diameter) in the nanodisc structure compared to the detergent structure. This expansion may result from environmental differences and influences interaction forces, thereby altering allosteric coupling.

In summary, the observed changes in inter-subunit packing interactions and ligand-binding cooperativity between nanodisc- and detergent-reconstituted HCN1 channels shows that the lipid membrane environment facilitates inter-subunit coupling between the transmembrane domain and the neighboring C-terminal domain, resulting in increased ligand-binding cooperativity in HCN channels in the closed conformation.

**Discussion:**

In this study, we investigate the role of lipid membranes in agonist binding to ion channels by reconstituting HCN1 and HCN4 channels in nanodiscs containing purified lipids and by extracting HCN1 directly from native membranes without detergent solubilization. To differentiate between competing models of cooperativity(*11, 12, 22, 62*), we directly measured the microscopic equilibrium constants associated with each of the four cAMP binding events using single-molecule methods. Our results show that the binding affinity of the first cAMP molecule is unaffected by the environment—whether in detergent or a lipid bilayer. However, subsequent cAMP binding events exhibit increased affinity for HCN channels in nanodiscs, whereas affinities remain unchanged for detergent-solubilized channels. This demonstrates that the lipid bilayer influences ligand-binding allostery, but not the intrinsic cAMP binding affinity.

To better mimic a native lipid environment and avoid detergent exposure, we directly extracted HCN1 channels into novel lipid-encapsulated nanodiscs(*59*) (DeFrNDs), bypassing the detergent solubilization step. Remarkably, cAMP binding to HCN1 channels in this system also displayed cooperative behavior, suggesting that the lipid bilayer plays a critical role in promoting positive cooperativity.

Comparing our HCN1 structure in soy lipid nanodiscs with previously solved detergent structures reveals a plausible mechanism for bilayer-dependent cooperativity. While the overall structural features remain consistent, the nanodisc-reconstituted structure shows subtle but significant differences: the intersubunit interfaces are more tightly packed in nanodiscs, with residue-residue distances at the interface between the S4-S5 linker and CNBD C-linker being, on average, 0.9 Å shorter. These structural changes are accompanied by a 1.3 Å expansion in the outer diameter of HCN1, indicating that tighter intersubunit packing likely contribute to cooperative behavior.

Similar changes were observed in a recently published higher-resolution (2.95 Å) HCN1 structure reconstituted in PC:PE nanodiscs, reinforcing this conclusion(*61*).

Our findings that the lipid bilayer increases intersubunit packing interactions and promotes cooperativity in HCN channels is consistent with the idea that solvating lipids in a bilayer as opposed to detergents reduce conformational flexibility, thereby destabilizing intermediate states and facilitating cooperative behavior. Membrane proteins solubilized in detergents have been found to be less stable compared to those reconstituted in nanodiscs(*61-63*). Similarly, single-molecule FRET measurements on β2-adrenergic receptors have shown that detergent-solubilized proteins undergo rapid transitions through a broad range of states in the presence of agonist, whereas receptors reconstituted in nanodiscs undergo slower transitions between active and inactive states(*63*).

The ability of lipid bilayers to promote cooperative binding without altering intrinsic affinity may have important physiological implications. Positive cooperativity acts as a gain factor in signaling pathways, amplifying small changes in signal while limiting the dynamic range. For HCN channels, enhancing cooperativity without changing intrinsic cAMP affinity enables lipid membranes to modulate signal amplification in pacemaker cells while preserving responsiveness to physiologically relevant cAMP concentrations. Future studies may reveal whether changes in lipid composition, due to aging, metabolic shifts, or disease, could modify or disrupt the integration of voltage- and cAMP-dependent signaling pathways.

**References**


1. C. Wahl-Schott, M. Biel, HCN channels: structure, cellular regulation and physiological function. *Cellular and molecular life sciences* **66**, 470-494 (2009).
2. R. B. Robinson, S. A. Siegelbaum, Hyperpolarization-activated cation currents: from molecules to physiological function. *Annual review of physiology* **65**, 453-480 (2003).
3. A. Ludwig, X. Zong, M. Jeglitsch, F. Hofmann, M. Biel, A family of hyperpolarization-activated mammalian cation channels. *nature* **393**, 587-591 (1998).
4. R. Gauss, R. Seifert, U. B. Kaupp, Molecular identification of a hyperpolarization-activated channel in sea urchin sperm. *Nature* **393**, 583-587 (1998).
5. B. Santoro *et al.*, Identification of a gene encoding a hyperpolarization-activated pacemaker channel of brain. *Cell* **93**, 717-729 (1998).
6. D. DiFrancesco, Pacemaker mechanisms in cardiac tissue. *Annual review of physiology* **55**, 455-472 (1993).
7. R. Gauss, R. Seifert, Pacemaker oscillations in heart and brain: a key role for hyperpolarization-activated cation channels. *Chronobiology international* **17**, 453-469 (2000).
8. D. DiFrancesco, P. Tortora, Direct activation of cardiac pacemaker channels by intracellular cyclic AMP. *Nature* **351**, 145-147 (1991).
9. V. Nache *et al.*, Activation of olfactory-type cyclic nucleotide-gated channels is highly cooperative. *The Journal of physiology* **569**, 91-102 (2005).
10. J. W. Karpen, A. L. Zimmerman, L. Stryer, D. A. Baylor, Gating kinetics of the cyclic-GMP-activated channel of retinal rods: flash photolysis and voltage-jump studies. *Proceedings of the National Academy of Sciences* **85**, 1287-1291 (1988).
11. J. Kusch *et al.*, Interdependence of receptor activation and ligand binding in HCN2 pacemaker channels. *Neuron* **67**, 75-85 (2010).
12. J. Kusch *et al.*, How subunits cooperate in cAMP-induced activation of homotetrameric HCN2 channels. *Nature chemical biology* **8**, 162-169 (2012).

13. D. T. Liu, G. R. Tibbs, P. Paoletti, S. A. Siegelbaum, Constraining ligand-binding site stoichiometry suggests that a cyclic nucleotide–gated channel is composed of two functional dimers. *Neuron* **21**, 235-248 (1998).
14. J. Li, H. A. Lester, Single-channel kinetics of the rat olfactory cyclic nucleotide-gated channel expressed in Xenopus oocytes. *Molecular pharmacology* **55**, 883-893 (1999).
15. J. Li, W. N. Zagotta, H. A. Lester, Cyclic nucleotide-gated channels: structural basis of ligand efficacy and allosteric modulation. *Quarterly reviews of biophysics* **30**, 177-193 (1997).
16. M. Lolicato *et al.*, Tetramerization dynamics of C-terminal domain underlies isoform-specific cAMP gating in hyperpolarization-activated cyclic nucleotide-gated channels. *Journal of Biological Chemistry* **286**, 44811-44820 (2011).
17. K. E. Hines, T. R. Middendorf, R. W. Aldrich, Determination of parameter identifiability in nonlinear biophysical models: A Bayesian approach. *Journal of General Physiology* **143**, 401-416 (2014).
18. T. R. Middendorf, M. P. Goldschen-Ohm, The surprising difficulty of "simple" equilibrium binding measurements on ligand-gated ion channels. *Journal of General Physiology* **154**, e202213177 (2022).
19. D. S. White, M. A. Smith, B. Chanda, R. H. Goldsmith, Strategies for Overcoming the Single-Molecule Concentration Barrier. *ACS Measurement Science Au* **3**, 239-257 (2023).
20. S. Peng, W. Wang, C. Chen, Breaking the Concentration Barrier for Single-Molecule Fluorescence Measurements. *Chemistry–A European Journal* **24**, 1002-1009 (2018).
21. P. Holzmeister, G. P. Acuna, D. Grohmann, P. Tinnefeld, Breaking the concentration limit of optical single-molecule detection. *Chemical Society Reviews* **43**, 1014-1028 (2014).
22. D. S. White *et al.*, cAMP binding to closed pacemaker ion channels is non-cooperative. *Nature* **595**, 606-610 (2021).
23. D. S. White, M. P. Goldschen-Ohm, R. H. Goldsmith, B. Chanda, Top-down machine learning approach for high-throughput single-molecule analysis. *Elife* **9**, e53357 (2020).
24. M. J. Levene *et al.*, Zero-mode waveguides for single-molecule analysis at high concentrations. *science* **299**, 682-686 (2003).
25. P. Zhu, H. G. Craighead, Zero-mode waveguides for single-molecule analysis. *Annual review of biophysics* **41**, 269-293 (2012).
26. J. Chen *et al.*, High-throughput platform for real-time monitoring of biological processes by multicolor single-molecule fluorescence. *Proceedings of the National Academy of Sciences* **111**, 664-669 (2014).
27. M. P. Goldschen-Ohm, D. S. White, V. A. Klenchin, B. Chanda, R. H. Goldsmith, Observing Single-Molecule Dynamics at Millimolar Concentrations. *Angewandte Chemie* **129**, 2439-2442 (2017).
28. S. Uemura *et al.*, Real-time tRNA transit on single translating ribosomes at codon resolution. *Nature* **464**, 1012-1017 (2010).
29. J. Hentschel *et al.*, Real-time detection of human telomerase DNA synthesis by multiplexed single-molecule FRET. *Biophysical journal* **122**, 3447-3457 (2023).
30. P. Pian, A. Bucchi, R. B. Robinson, S. A. Siegelbaum, Regulation of gating and rundown of HCN hyperpolarization-activated channels by exogenous and endogenous PIP2. *The Journal of general physiology* **128**, 593-604 (2006).
31. P. A. Schmidpeter *et al.*, Anionic lipids unlock the gates of select ion channels in the pacemaker family. *Nature structural & molecular biology* **29**, 1092-1100 (2022).
32. C. J. daCosta, L. Dey, J. P. Therien, J. E. Baenziger, A distinct mechanism for activating uncoupled nicotinic acetylcholine receptors. *Nat Chem Biol* **9**, 701-707 (2013).

33. R. Rusinova, C. He, O. S. Andersen, Mechanisms underlying drug-mediated regulation of membrane protein function. *Proc Natl Acad Sci U S A* **118**, (2021).
34. I. Levental, E. Lyman, Regulation of membrane protein structure and function by their lipid nano-environment. *Nat Rev Mol Cell Biol* **24**, 107-122 (2023).
35. B. Reddy, N. Bavi, A. Lu, Y. Park, E. Perozo, Molecular basis of force-from-lipids gating in the mechanosensitive channel MscS. *Elife* **8**, (2019).
36. E. Perozo, D. M. Cortes, P. Sompornpisut, A. Kloda, B. Martinac, Open channel structure of MscL and the gating mechanism of mechanosensitive channels. *Nature* **418**, 942-948 (2002).
37. Y. Zhang *et al.*, Visualization of the mechanosensitive ion channel MscS under membrane tension. *Nature* **590**, 509-514 (2021).
38. H. Zheng, W. Liu, L. Y. Anderson, Q.-X. Jiang, Lipid-dependent gating of a voltage-gated potassium channel. *Nature communications* **2**, 250 (2011).
39. C. Yuan, R. J. O'Connell, R. F. Jacob, R. P. Mason, S. N. Treistman, Regulation of the gating of BKCa channel by lipid bilayer thickness. *Journal of Biological Chemistry* **282**, 7276-7286 (2007).
40. H. X. Zhou, T. A. Cross, Influences of membrane mimetic environments on membrane protein structures. *Annu Rev Biophys* **42**, 361-392 (2013).
41. C. R. Sanders, K. F. Mittendorf, Tolerance to changes in membrane lipid composition as a selected trait of membrane proteins. *Biochemistry* **50**, 7858-7867 (2011).
42. V. R. Patel *et al.*, Single-molecule imaging with cell-derived nanovesicles reveals early binding dynamics at a cyclic nucleotide-gated ion channel. *Nature Communications* **12**, 6459 (2021).
43. M. P. Goldschen-Ohm *et al.*, Structure and dynamics underlying elementary ligand binding events in human pacemaking channels. *Elife* **5**, e20797 (2016).
44. J. Larson *et al.*, Design and construction of a multiwavelength, micromirror total internal reflectance fluorescence microscope. *Nature protocols* **9**, 2317-2328 (2014).
45. A. Bandyopadhyay, M. P. Goldschen-Ohm, Unsupervised selection of optimal single-molecule time series idealization criterion. *Biophysical Journal* **120**, 4472-4483 (2021).
46. G. S. Adair, A. Bock, H. Field Jr, The hemoglobin system: VI. The oxygen dissociation curve of hemoglobin. *Journal of Biological Chemistry* **63**, 529-545 (1925).
47. C.-L. Huang, S. Feng, D. W. Hilgemann, Direct activation of inward rectifier potassium channels by PIP2 and its stabilization by Gβγ. *Nature* **391**, 803-806 (1998).
48. N. Gamper, M. S. Shapiro, Regulation of ion transport proteins by membrane phosphoinositides. *Nature Reviews Neuroscience* **8**, 921-934 (2007).
49. T. Rohacs, Phosphoinositide regulation of TRP channels. *Mammalian Transient Receptor Potential (TRP) Cation Channels: Volume II*, 1143-1176 (2014).
50. D. W. Hilgemann, S. Feng, C. Nasuhoglu, The complex and intriguing lives of PIP2 with ion channels and transporters. *Science's STKE* **2001**, re19-re19 (2001).
51. A. A. Rodríguez-Menchaca, S. K. Adney, L. Zhou, D. E. Logothetis, Dual regulation of voltage-sensitive ion channels by PIP2. *Frontiers in pharmacology* **3**, 170 (2012).
52. M. Kruse, G. R. Hammond, B. Hille, Regulation of voltage-gated potassium channels by PI (4, 5) P2. *Journal of general physiology* **140**, 189-205 (2012).
53. V. Dalal *et al.*, Lipid nanodisc scaffold and size alter the structure of a pentameric ligand-gated ion channel. *Nature communications* **15**, 25 (2024).
54. S. Ganapathy *et al.*, Membrane matters: The impact of a nanodisc-bilayer or a detergent microenvironment on the properties of two eubacterial rhodopsins. *Biochimica et Biophysica Acta (BBA)-Biomembranes* **1862**, 183113 (2020).

55. S. Zhang *et al.*, One-step construction of circularized nanodiscs using SpyCatcher-SpyTag. *Nature communications* **12**, 5451 (2021).
56. I. Schachter, C. Allolio, G. Khelashvili, D. Harries, Confinement in nanodiscs anisotropically modifies lipid bilayer elastic properties. *The Journal of Physical Chemistry B* **124**, 7166-7175 (2020).
57. M. Daniilidis, M. J. Brandl, F. Hagn, The advanced properties of circularized MSP nanodiscs facilitate high-resolution NMR studies of membrane proteins. *Journal of Molecular Biology* **434**, 167861 (2022).
58. A. Moroni *et al.*, Hyperpolarization-activated cyclic nucleotide-gated channel 1 is a molecular determinant of the cardiac pacemaker current I f. *Journal of Biological Chemistry* **276**, 29233-29241 (2001).
59. Q. Ren *et al.*, DeFrND: detergent-free reconstitution into native nanodiscs with designer membrane scaffold peptides. . *bioRxiv*, (2024).
60. C.-H. Lee, R. MacKinnon, Structures of the human HCN1 hyperpolarization-activated channel. *Cell* **168**, 111-120. e111 (2017).
61. E. D. Kim *et al.*, Propofol rescues voltage-dependent gating of HCN1 channel epilepsy mutants. *Nature* **632**, 451-459 (2024).
62. S. Kuschke *et al.*, cAMP binding to closed pacemaker ion channels is cooperative. *Proceedings of the National Academy of Sciences* **121**, e2315132121 (2024).
63. R. Lamichhane *et al.*, Single-molecule view of basal activity and activation mechanisms of the G protein-coupled receptor β2AR. *Proceedings of the National Academy of Sciences* **112**, 14254-14259 (2015).

**Acknowledgments:** The fabrication of the ZMW waveguides was conducted as part of a user project at the Center for Nanophase Materials Sciences (CNMS), a US Department of Energy, Office of Science User Facility at Oak Ridge National Laboratory.
The authors would like to acknowledge guidance and training in the fabrication process by Bernadeta Srijanto, Dale Hensley, Daryl Briggs, Kevin Lester, Leslie Wilson, and Scott Retterer.
Cryo-EM data were collected at the Washington University Center for Cellular Imaging (WUCCI), supported by the Washington University School of Medicine, The Children's Discovery Institute of Washington University, and St. Louis Children's Hospital (CDI-CORE-2015-505 and CDI-CORE-2019-813) and the Foundation for Barnes-Jewish Hospital (3770 and 4642).
We thank Drs. B. Summers and K. Basore at WUCCI for grid freezing and help with cryo-EM data collection. We thank Drs. W. Cheng and A.S. Evers for discussion and comments.

**Funding:**
National Institutes of Health grant NS101723 (B.C)
National Institutes of Health grant DP2GM140920 (H.B)
National science foundation grant CHE-1856518 (R.H.G)

**Author contributions:**
Conceptualization: B.C, R.H.G, H.B, V.I, S.R.C
Experiments: V.I, S.R.C, Y.C, Q.R
Writing and editing – B.C, R.H.G, H.B, V.I, S.R.C

**Competing interests:** Authors declare that they have no competing interests.
**Data and materials availability:** All data, code, and materials used in the analysis will be made available to any researcher for purposes of reproducing or extending the analysis.

**Supplementary Materials**
Materials and Methods
Figs. S1 to S17
Tables S1 to S35
**Other Supplementary Materials for this manuscript include the following**
Movies S1 and S2

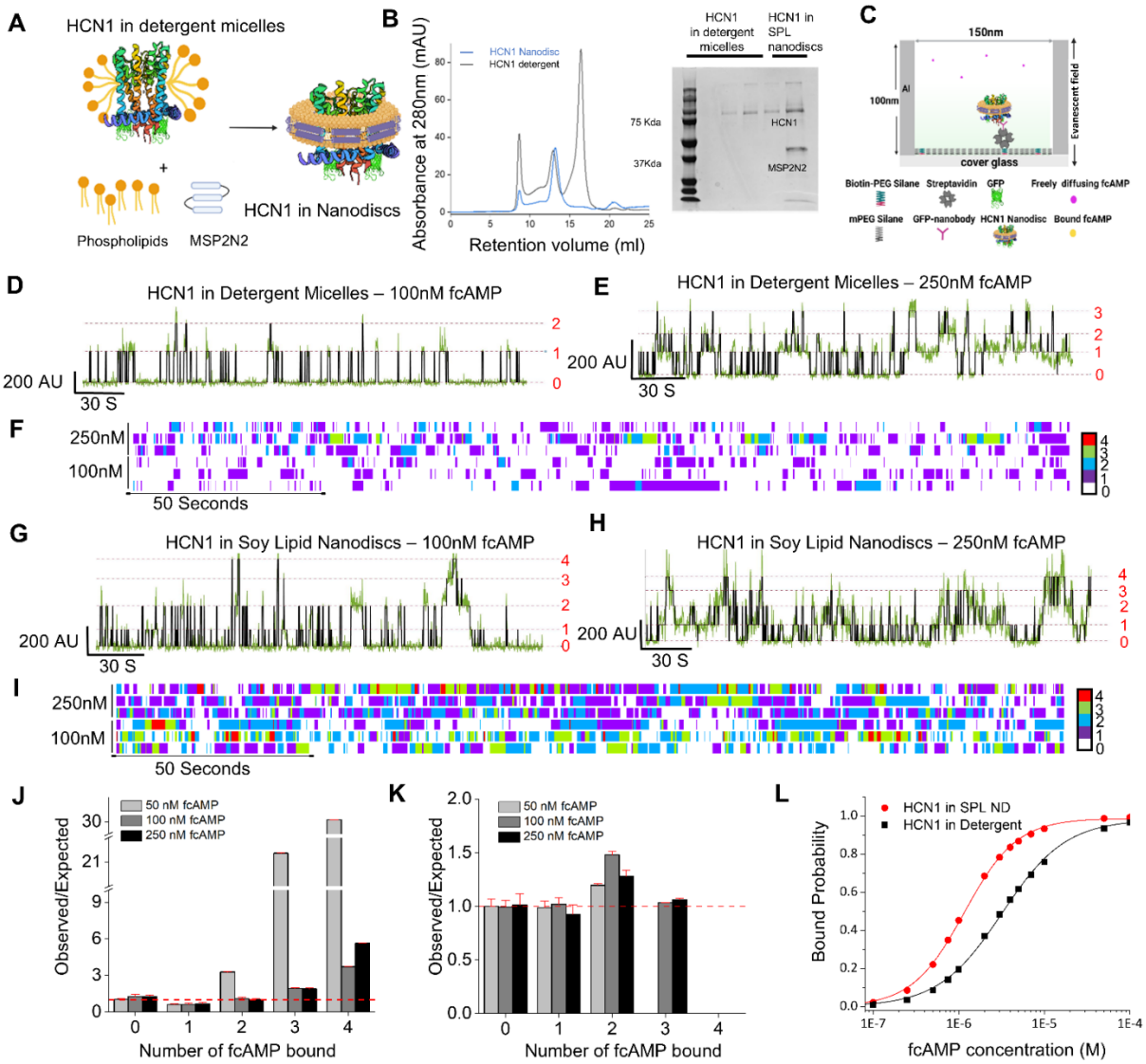


**Fig. 1. Ligand-binding activity in nanodisc-reconstituted and detergent-solubilized HCN channels. (A)** Schematic of HCN1 reconstitution into lipid nanodiscs using MSP2N2 as scaffold protein (1:2.5:200 ratio of HCN1, MSP2N2, and soy polar lipids). **(B)** (left) Size exclusion chromatography profile of HCN1 purified in detergent (blue) and HCN1 purified in detergent and reconstituted into soy polar lipid nanodiscs with MSP2N2 (black). (right) Coomassie blue stained SDS-PAGE gel showing various SEC fractions of HCN1 at ~75Kda before reconstitution (lanes 2-4) and both HCN1 and MSP bands after reconstitution (lane 5) **(C)** Cartoon (not to scale) of single-molecule pulldown of HCN1 onto a ZMW. ZMWs passivated with mPEG silane doped with biotin-PEG-silane and coated with streptavidin. Biotinylated GFP pulled down GFP-tagged HCN1. **(D, E)** Representative FT traces of 100 nM fcAMP (**D**) and 250 nM fcAMP (**E**) binding to HCN1 in a detergent micelle. Dashed lines, ligated state of the channel. **(F)** Heatmap of three independent FT traces of 100 nM and 250 nM fcAMP binding to HCN1 in detergent micelles. **(G, H)** Representative FT traces of 100 nM and 250 nM fcAMP binding to HCN1 in soy polar lipid nanodiscs. **(I)** Heatmap of three independent FT traces of 100 nM and 250 nM fcAMP binding to HCN1 in soy polar lipid nanodiscs. **(J, K)** Ratios of observed ($P(k)_{obs}$) and expected ($P(k)_{exp}$) values of liganded state occupancies from binomial fits across all trajectories for HCN1 in soy

polar lipid nanodiscs (**J**) or detergent micelles (**K**) at different fcAMP concentrations. Red dashed line, concordance between observed and expected values; error bars (red), standard deviation. Soy polar lipid nanodiscs, N = 945 molecules; total observation time 112.24 hours; total events 234859 (table S1). Detergent, N = 579 molecules; total observation time 50.5 hours; total events 106542 (table S2). **(L)** Extrapolated binding curve for HCN1 in soy polar lipid nanodiscs (black) and detergent (red) generated by calculating predicted bound probability from experimentally obtained microscopic equilibrium rate constants and substituting them in Adair's equation for four binding sites(*46*).

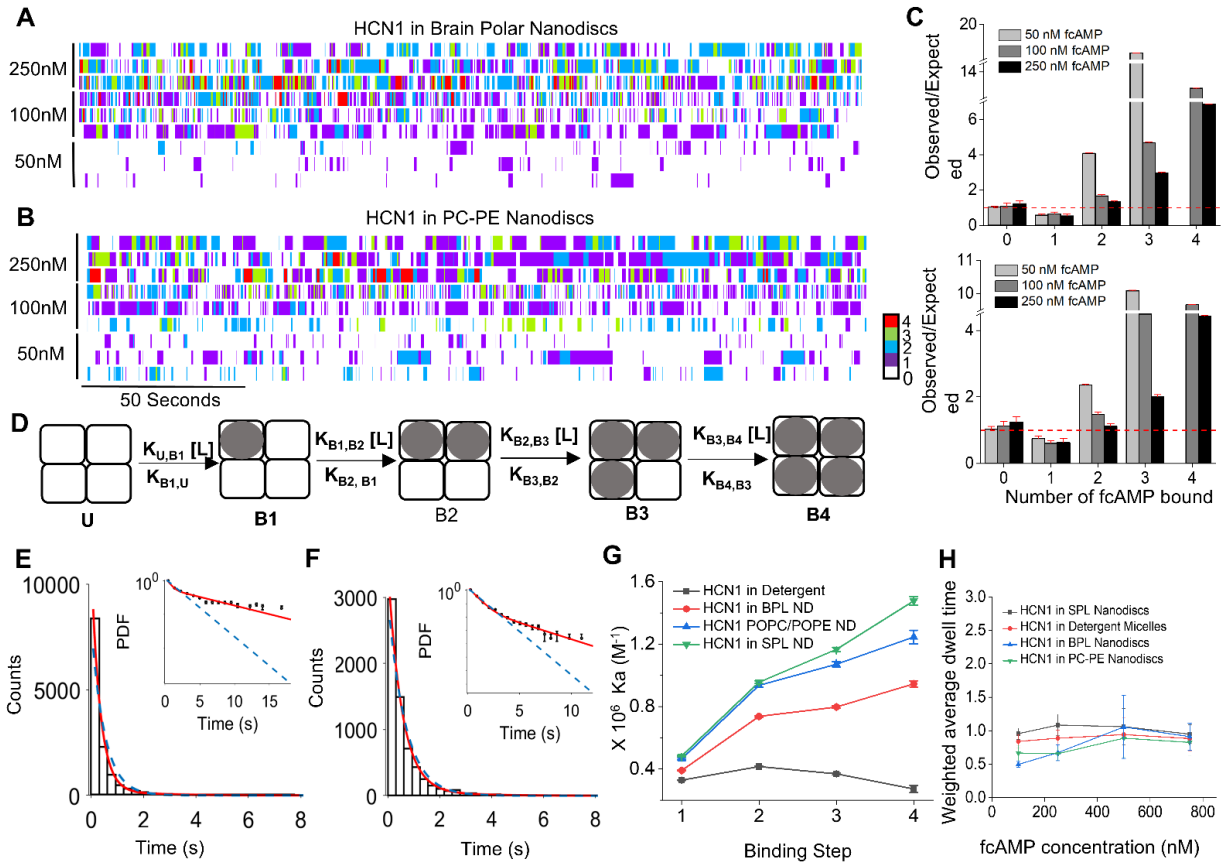


**Fig. 2**. **Lipid bilayer effect on microscopic binding affinities for higher-order ligation states.** **(A, B)** Heatmap of three independent FT traces of 50 nM, 100 nM, and 250 nM fcAMP binding to HCN1 reconstituted in (**A**) porcine brain polar lipid nanodiscs and (**B**) POPC/POPE lipid nanodiscs. **(C)** Ratios of $P(k)_{obs}$ and $P(k)_{exp}$ for liganded state occupancies from binomial fits across all trajectories for HCN1 in brain polar lipid nanodiscs (top) and a 3:1 ratio of POPC/POPE (bottom) at different fcAMP concentrations. Brain polar lipid nanodiscs, N = 898 molecules; total observation time = 90.24 hours; total events = 238280. POPC/POPE nanodiscs, N = 372 molecules; total observation time = 51.2 hours, total events = 141600. See tables S3 and S4. (**D**) Schematic of sequential model for ligand binding. White squares unbound (U); squares with grey circles, bound (B) ligand. **(E, F)** Dwell time distributions of isolated UBU events for HCN1 in (**E**) brain polar lipid nanodiscs and (**F**) POPE/POPE nanodiscs at 100 nM fcAMP. Distributions overlaid with maximum likelihood estimates for monoexponential (blue dashed) and bi-exponential (red) distributions. Error bars denote standard deviation. Individual time constants and amplitudes in table S21, S22. **(G)** Microscopic equilibrium association constants (Ka) for each ligation state of HCN1 in Soy polar lipid nanodiscs, POPC/POPE nanodiscs, brain polar lipid nanodiscs, and detergent micelles. Parameters obtained by global fitting to all events across all concentrations for each condition. **(H)** Biexponential weighted dwell time constant of the first bound state at various fcAMP concentrations obtained by fitting UBU dwell times with a biexponential function.

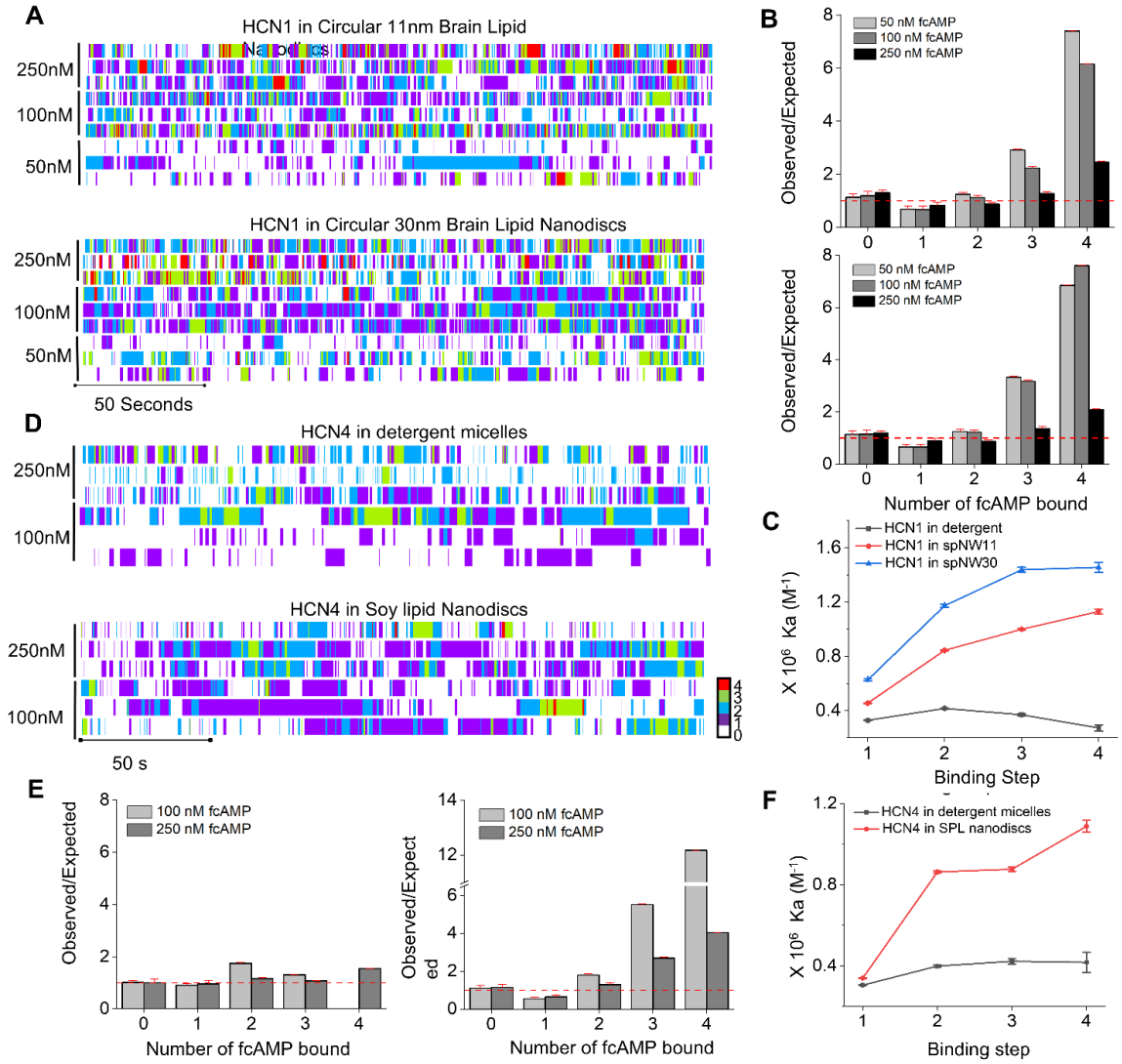


**Fig. 3. Ligand-binding cooperativity in different-sized circular nanodiscs and HCN4 isoform.** **(A)** Heatmap of three independent FT traces of 100 nM, 250 nM, and 750 nM fcAMP binding to HCN1 reconstituted in 11 nm (spMSP1D1, top) and 30 nm (spNW30, bottom) circular nanodiscs of brain polar lipids. **(B)** Ratios of $P(k)_{obs}$ and $P(k)_{exp}$ for liganded state occupancies from binomial fits across all trajectories for HCN1 reconstituted into 11 nm (top) and 30 nm (bottom) circular nanodiscs of brain polar lipids at 50 nM, 100 nM and 250 nM fcAMP. 11 nm circular nanodiscs, N = 743 molecules; total observation time 122.3 hours; total events 379403. 30 nm circular nanodiscs, N = 461 molecules; total observation time 76.4 hours; total events 198934. See tables S5 and S6. **(C)** Heatmap of three independent FT traces of 100 nM and 250 nM fcAMP binding to HCN4 in GDN detergent micelles (top) and soy polar lipid nanodiscs (bottom). **(D)** Ratios of $P(k)_{obs}$ and $P(k)_{exp}$ for liganded state occupancies from binomial fits across all trajectories for HCN4 reconstituted in detergent micelles (top) and soy polar lipid nanodiscs (bottom) at 100 nM and 250 nM fcAMP. Detergent micelles, N = 517 molecules; total observation time 43.08 hours; total events 43982. Soy polar lipid nanodiscs, N = 498 molecules; total observation time 58 hours; total events 97429. See tables S7 and S8. **(E)** Ka values for all tested conditions showing positive cooperativity for HCN1 in both 11 nm and 30 nm nanodiscs, and independent binding in detergent micelles. Parameters obtained by fitting an optimized unconstrained sequential model to all events

across all concentrations. **(F)** Ka values for all tested conditions showing positive cooperativity for HCN4 in soy lipid nanodiscs and independent binding in detergent micelles. Parameters fit to all events across all concentrations.

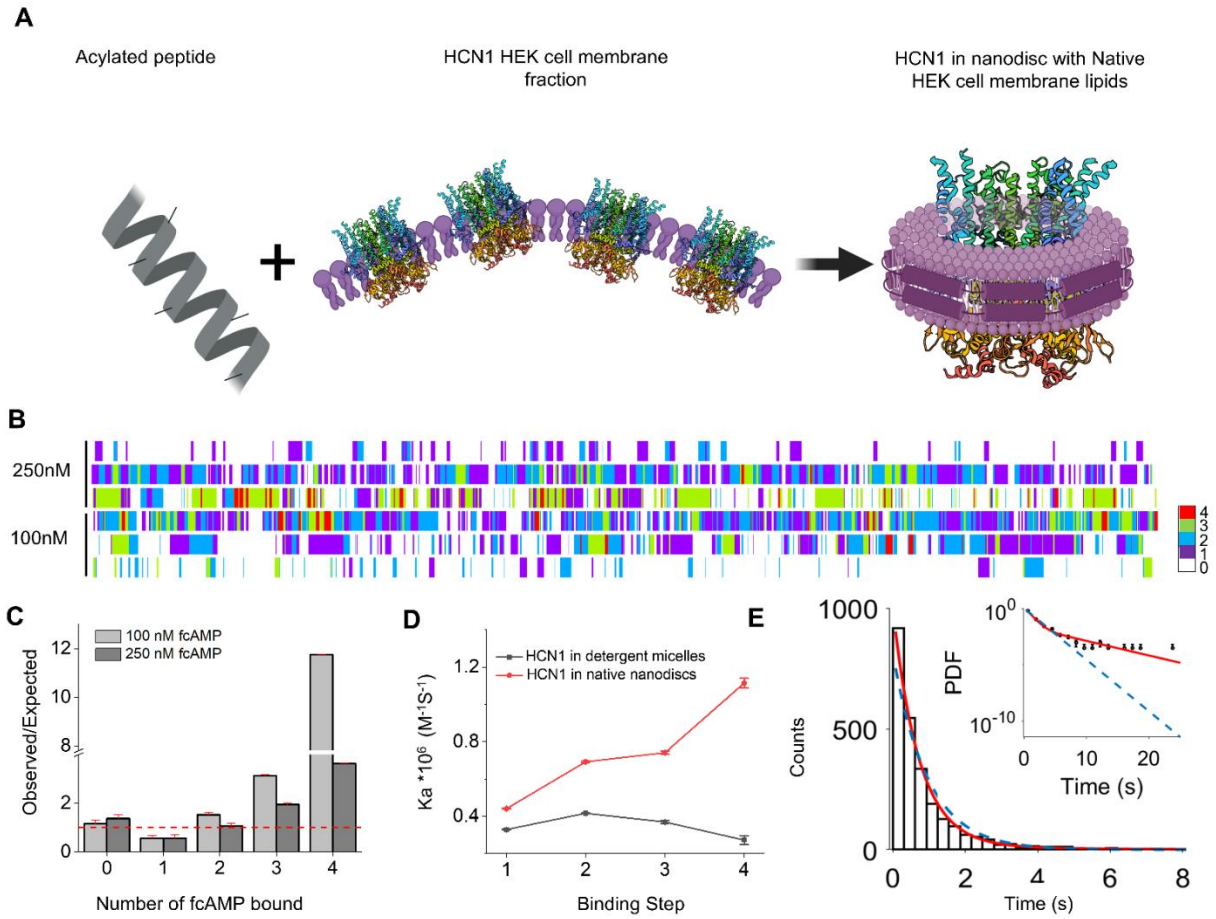


**Fig. 4**. **HCN channels purified in native nanodiscs show cooperative fcAMP binding.** **(A)** Schematic of HCN1 reconstitution into native HEK cell nanodiscs using acylated peptides as a MSP. **(B)** Ratios of $P(k)_{obs}$ and $P(k)_{exp}$ for liganded state occupancies from binomial fits across all trajectories for HCN1 in native HEK membrane lipid nanodiscs at 100nM and 250nM fcAMP. **(C)** Heatmap of three independent FT traces of 100nM and 250nM fcAMP binding to HCN1 purified in native HEK cell nanodiscs. **(D)** Ka values for all tested conditions showing positive cooperativity for HCN1 in native lipid nanodiscs and independent binding in detergent micelles. Parameters fit to all events across all concentrations. Native HEK cell nanodiscs, N = 671 molecules. See table S9. **(E, F)** Dwell time distributions of isolated B1 events for HCN1 in native HEK cell nanodiscs at 100nM (**E**) fcAMP. Distributions overlaid with maximum likelihood estimates for monoexponential (blue dashed) and bi-exponential (red) distributions. Error bars are for a binomial distribution. Individual time constants and amplitudes in table S25.

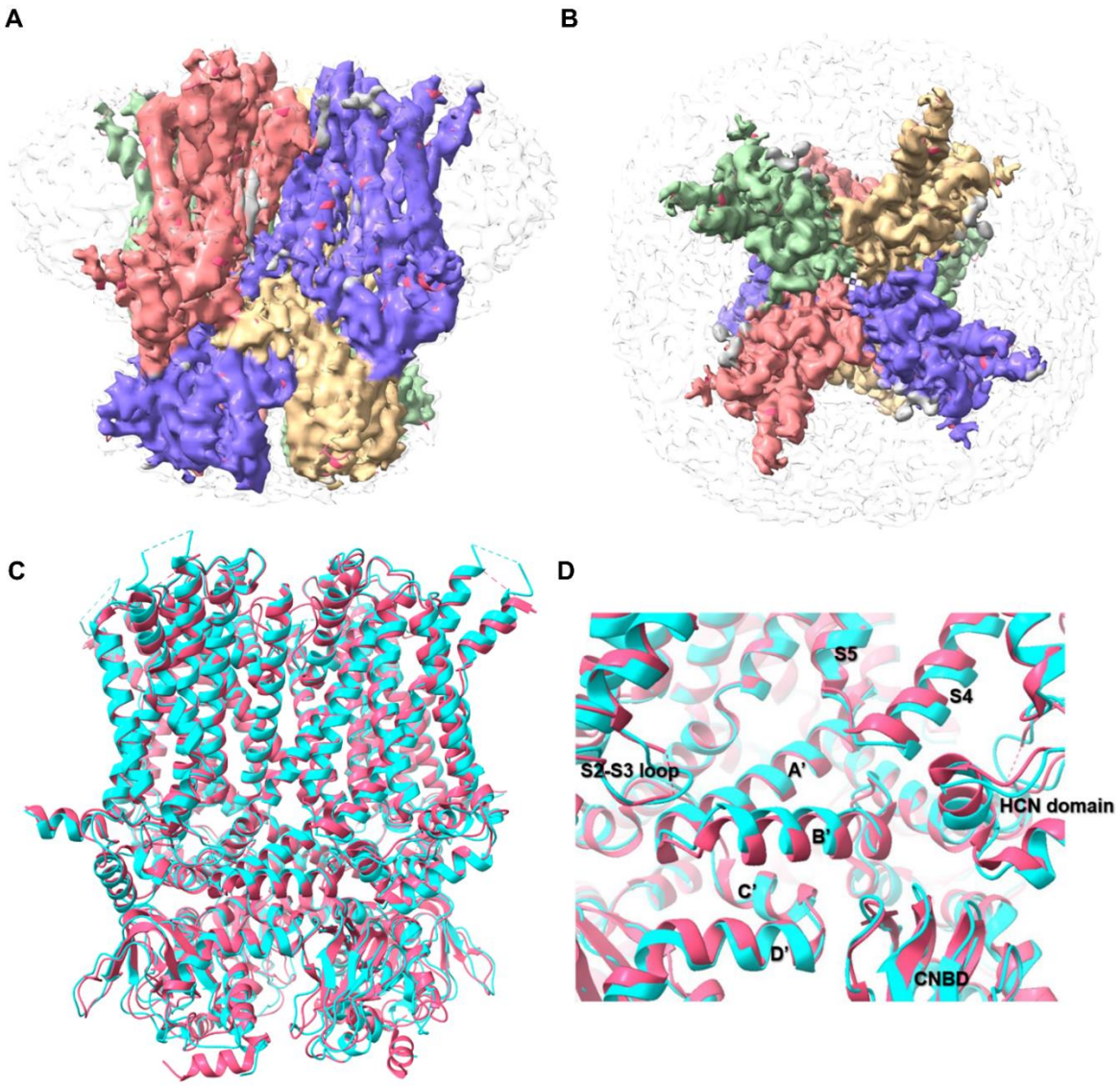


**Fig. 5. Cryo-EM structure of hHCN1 in soy polar lipid nanodisc.** **(A**) Side-view of hHCN1 cryo-EM map colored with the superimposed model subunits. **(B)** Superimposed models of hHCN1-nanodisc (cyan) and hHCN1-detergent (PDB: 5u6o, red) zoomed in to the region with inter-subunit interactions. **(C)** Comparison of hHCN1-nanodisc and hHCN1-detergent at the interface between S4-S5/HCN and C-terminal domain (including C-linker and CNBD). Left: structural models with ribbon presentation; Right: structural models with surface presentation. Note that a small upward movement of A'-B' of the C-linker and CNBD and a small downward movement of HCN domain and S4-S5 loop. **(D)** Comparison of hHCN1-nanodisc and hHCN1-detergent at the interface between C'-D' of the C-linker and C-terminal domain (including A'-B' of the C-linker on the upper left and CNBD on the upper right).

**Table 1. Molar Ratios of HCN1, scaffold proteins and lipids for various nanodisc reconstitution assays**

| Protein | Scaffolding protein | Lipids | Molar Ratio (Protein: MSP: Lipid) |
|---|---|---|---|
| HCN1 | MSP2N2 | Soy Polar lipids | 1:2.5:200 |
| HCN1 | MSP2N2 | POPC/POPE | 1:2.5:280 |
| HCN1 | MSP2N2 | Brain Polar lipids | 1:2.5:200 |
| HCN1 | spNW11 | Brain Polar lipids | 1:2.5:95 |
| HCN1 | spNW30 | Brain Polar lipids | 1:2.5:600 |
| HCN4 | MSP2N2 | Soy Polar lipids | 1:2.5:200 |

**Table 2. Imaging parameters for CryoEM data acquisition.**

| | Dataset 1 | Dataset2 | Dataset3 |
|---|---|---|---|
| Surfactant | no | no | 0.2mM Fl-fos-choline |
| Tilting (°) | 30 | 30 | 0 |
| Accelerating Voltage (kV) | 200 | 200 | 200 |
| Pixel Size (Å) | 1.184 | 1.184 | 1.184 |
| Spherical Aberration (mm) | 2.7 | 2.7 | 2.7 |
| Total Dose (e/Å$^2$) | 47.9 | 43.13 | 50.63 |
| Fractions | 40 | 40 | 45 |
| Number of micrographs | 279 | 489 | 6993 |